Biosensors and Bioelectronics 144 (2019) 111691

Contents lists available at ScienceDirect

Biosensors and Bioelectronics

journal homepage: www.elsevier.com/locate/bios

Ultrasensitive electrochemical sensor for prostate specific antigen detection with a phosphorene platform and magnetic covalent organic framework signal amplifier

Huan Liang[a,1], Hanbin Xu[a,1], Yuting Zhao[a], Jing Zheng[a], Hui Zhao[b,***], Guoliang Li[c,**], Can-Peng Li[a,*]

[a] School of Chemical Science and Technology College of Pharmacy, Yunnan University, Kunming, 650091, PR China
[b] Laboratory for Conservation and Utilization of Bio-resource, Yunnan University, Kunming, 650091, PR China
[c] School of Food and Biological Engineering, Shaanxi University of Science and Technology, Xi'an, 710021, PR China

ARTICLE INFO

Keywords:
Electrochemical immunosensor
Magnetic covalent organic framework
Phosphorene
Prostate specific antigen

ABSTRACT

Magnetic covalent organic frameworks (COFs) are useful mesoporous materials for the enrichment and separation of analytes, and are utilized in the pretreatment of samples. However, the use of magnetic COFs in electrochemical immunosensors has rarely reported. Herein, a novel electrochemical assay for the determination of prostate specific antigen (PSA) was developed using black phosphorene (BPene) as a platform and magnetic COFs for signal amplification. BPene was prepared via water-phase exfoliation. BPene nanocomposite (Au@BPene) was prepared by depositing Au nanoparticles (Au NPs) onto BPene. This nanocomposite was utilized as an immunsensing platform to bind primary antibodies and improve electron transfer. Subsequently, an Au NP-loaded magnetic COF was used to immobilize the secondary antibodies and abundant electronic signals of methylene blue (MB). The fabricated sensor exhibited linearity ranging from 0.0001 ng mL^{-1} to 10 ng mL^{-1} with the detection limit of 30 fg mL^{-1}. The sensor could determine the PSA in a real sample with excellent specificity, good stability, and desirable reproducibility. The effective signal amplification of the proposed sensor is attributed to the good electron transfer of Au@BPene, excellent enrichment capacity of signal molecules (MB) of the COF, and efficient catalytic activity of Fe_3O_4. This work not only provides an effective electrochemical assay to detect PSA in real sample, but also broadens the utilization scope of magnetic COFs in immunosensing.

1. Introduction

Prostate cancer is a malignant tumor in male prostate tissue, and is the third main cause of cancer mortality in males (Center et al., 2012). In the United State, approximately 14% of males are diagnosed with prostate cancer in their whole lifetime. However, thus far, there has been no perfect radical treatment for prostate cancer (Pei et al., 2015). The prostate specific antigen (PSA) is the most effective serum biomarker available for screening and diagnosing prostate tumors (Yang et al., 2018). The PSA concentration in serum for a healthy male is 0–4.0 ng mL^{-1}, and the concentration above of 10 ng mL^{-1} are considered as abnormal (Jin et al., 2015). It is well-known that PSA detection can screen the initial prostate cancer in symptomless males group. This is helpful for reducing the mortality rate and prolonging the life span of prostate cancer patients (Cooperberg et al., 2018). Therefore, the sensitive detection of PSA is vital in the prediction and diagnosis of prostate cancer. For PSA determination, various methods such as radioimmunoassay (Teppo and Maury, 1987), fluorescence immunoassay (Pei et al., 2015), chemiluminescence immunoassay (Cesaro-Tadic et al., 2004), surface-enhanced Raman scattering-based immunoassay (Cheng et al., 2017), and plasmonic enzyme-linked immunosorbent assay (ELISA) (Xuan et al., 2016) have been developed. However, these methods still present some drawbacks, in terms of the expensive instruments, time-consuming process, low effectiveness, or long measurement procedures, which hinder their clinical application. Therefore, it is imperative to develop a fast, efficient, and simple

* Corresponding author.
** Corresponding author.
*** Corresponding author.
E-mail addresses: zhaohui@ynu.edu.cn (H. Zhao), 61254368@163.com (G. Li), lcppp1974@sina.com (C.-P. Li).
[1] These authors contributed equally to this work.

https://doi.org/10.1016/j.bios.2019.111691
Received 6 July 2019; Received in revised form 5 September 2019; Accepted 6 September 2019
Available online 08 September 2019
0956-5663/

analytical approach for PSA measurement.

Phosphorene (BPene) is an important two-dimensional (2D) material of monolayer black phosphorus (BP), and has attracted immense research attention owing to its unique structure and attractive photoelectric properties (Ge et al., 2019). BPene was first prepared from bulk BP in 2014 (Li et al., 2014). In BPene, every phosphorus atom is linked with three neighbouring phosphorus atoms to form a puckered honeycomb structure, with a space of ~ 5 Å between two layers. The two neighbouring layers of BP are stacked on each other by van der Waals interactions (Luo et al., 2019). This unique structure provides BPene with attractive electronic properties, such as high mobility, anisotropic electrical and thermal conductivity, and superior optical response. Therefore, BPene has been the 2D material of choice in biomedicine, bioimaging, biosensing, and theranostics (Ge et al., 2019; Luo et al., 2019). Recently, much pioneering work on chemical sensors has been performed based on BPene or its nanocomposite for gas sensing, ion sensing, or other small-molecule sensing application (Li et al., 2015, 2017). However, the exploration of BPene for biosensing is still limited (Zhao et al., 2018). Particularly, less effort has been invested toward investigating BPene-based immunosensors.

Covalent organic frameworks (COF) are porous material with highly regular 2D or 3D networks, which are formed by the linkage of organic molecular building units via reversible covalent bonds (Côté et al., 2005; Colson and Dichtel, 2013). Owing to their intriguing structure and unique properties, COFs have been widely adopted in gas storage or separation, catalysis, photovoltaic conversion, and drug delivery (Ding et al., 2011; Li et al., 2012; Fang et al., 2014). Recently, electrochemical sensors based on COFs or their composites have been developed owing to their tunable pore size and shapes, large surface area, easily customizable functionalities, and good thermal stability (Liu et al., 2016b; Zhang et al., 2018; Yan et al., 2019). These unique properties offer noteworthy opportunities for advanced utilization in sensing. More recently, magnetic COF was synthesized for the enrichment and separation of target analytes and further used in some analytical technologies (Li et al., 2018; He et al., 2017; Wang et al., 2017), which simplified the process of sample pretreatment. However, there are few reports on the use of COFs in biosensing fields (Yan et al., 2019; Liu et al., 2016a). To our best knowledge, there has been no report thus far on immunosensors using magnetic COFs.

Previous investigations indicated that a magnetic Fe_3O_4/reduced graphene oxide composite can be successfully utilized to fabricate ultrasensitive biosensor for nucleic acid-based biomarkers. In this biosensor, magnetic Fe_3O_4 played a catalytic role toward the probe molecule and efficiently amplified the signal (Zhao et al., 2017; Wen et al., 2014). Furthermore, methylene blue (MB) is an aromatic heterocyclic dye, and has been frequently used in electrochemical sensors and biosensors as a reliable redox probe. MB can be incorporated into the cavity of macrocyclic supramolecular hosts, such as calixarene and pillararene, to form a stable host–guest complex via multi−-noncovalent interactions, such as $\pi-\pi$ stacking, electrostatic interaction, and hydrophobic interaction (Zhao et al., 2017, 2019; Yang et al., 2016). These host–guest interactions favor the enrichment of the signal molecule (MB), and therefore amplify the signal. It is well-known the pore of COFs has a benzene ring-containing ligand, which can be regarded as a macrocyclic supramolecular host. Hence, aromatic guest molecules can be included by COFs (Li et al., 2018; Wang et al., 2017). Inspired by these interesting results, we speculated that magnetic COFs may amplify electrochemical signals due to the excellent enrichment capacity and catalytic activity towards the probe molecule.

In this study, we are the first to design and develop a novel electrochemical assay for PSA determination using BPene as the substrate material and the magnetic COF as the nanoprobe for the generation and amplification of electrochemical signals. Our fabricated immunosensor exhibited low detection limit, fine specificity, and good stability. This work not only provides an effective electrochemical assay to determine the PSA in real samples, but also broadens the application scope of BPene and magnetic COFs in biosensing.

2. Materials and methods

2.1. Materials and reagents

The PSA, PSA antibody (Ab1 and Ab2), carcino-embryonic antigen (CEA), and human serum were obtained from Biocell Co., Ltd. (Zhengzhou, China). Gold chloride hydrate ($HAuCl_4$), potassium hexacyanoferrate (III) ($K_3Fe(CN)_6$), potassium hexacyanoferrate (II), methylene blue (MB), tetrahydrofuran (THF), benzidine (BD), 1,3,5-triformylphloroglucinol (Tp), bovine serum albumin (BSA), ovalbumin (OVA), human immunoglobin G (hIgG), lysozyme (Lz), human serum albumin (HSA), and C-reaction protein (CRP) were obtained from Adamas-beta Reagent Co., Ltd. (Shanghai, China). PSA ELISA kit was purchased from Abnova Corporation (Walnut, CA, USA). In this work, 0.1 M of PBS was used at pH 7.2. All other reagents above were analytical-grade and used without further purification. All aqueous solutions were prepared with deionized water (DW, 18 MΩ cm^{-1}).

2.2. Apparatus

The morphologies of the prepared samples were characterized by scanning electron microscopy (SEM; QUNT200, USA) and transmission electron microscopy (TEM; JEM 2100, Japan) with energy dispersive X-ray spectroscopy (EDX). Fourier transform infrared (FTIR) characterization was performed over the wavenumber range of 4000–400 cm^{-1} using a Thermo Fisher Scientific Nicolet IS10 (Massachusetts, USA) FTIR Impact 410 spectrophotometer with KBr pellets. Raman spectra were obtained on a 400F Perkin–Elmer Raman spectrometer (Shelton, USA) with incident laser light of wavelength 514.5 nm. X-ray photoelectron spectroscopy (XPS) measurements were performed with Al Kα X-ray radiation as the X-ray source for excitation, on an ESCALAB-MKII spectrometer (VG Co., United Kingdom). The obtained samples were characterized by mapping using a Tecnai G2 F20 (FEI Co., United States). Zeta potential measurements were performed using a model Zetasizer Nano ZS instrument (Malvern Instruments, Worcestershire, UK) with a disposable polycarbonate folded capillary cell (model DTS1070) of path length 4 mm. The zeta potential values are reported as the mean of three measurements.

2.3. Preparation of black phosphorene (BPene) and Au nanoparticles loaded BPene (Au@BPene)

BPene was synthesized via liquid ultrasonic exfoliation from a bulk BP sample according to a previous method reported by Zeng et al. (2018). Typically, 10 mg of bulk BP powder was added to 20 mL oxygen-free water and then sonicated in an ice bath for 6 h. Subsequently, the resulting light brown suspension was centrifugated at 3000 rpm for 10 min to get rid of the residual unexfoliated bulk BP particles, and the supernatant was collected by centrifugation at 9000 rpm for 15 min. The BPene powder was obtained by freeze drying. The Au NPs employed in this work were obtained through the reduction of $HAuCl_4$ by citric acid. Briefly, 1.07 mL of 23.46 mM $HAuCl_4$ was added to 100 mL of boiling deionized water under vigorous stirring. This mixture was continuously stirred at 110 °C for 10 min. Subsequently, 10 mL of 14.55 mM sodium citrate solution was successively added and refluxed for 25-35 min till the color of the solution turned into wine red. This solution was then boiled under agitation at room temperature for 15 min to ensure completion of the reaction. Finally, the solution was naturally cooled to room temperature. The structural transformation from bulk BP to BPene was investigated by Raman spectroscopy. The thickness of the exfoliated BPene was determined by atomic force microscopy.

To prepare Au@BPene, 200 μL of 1.0 mg ml^{-1} BPene was added to 2 mL of the above-prepared Au NPs dispersion and stirred at 4 °C for

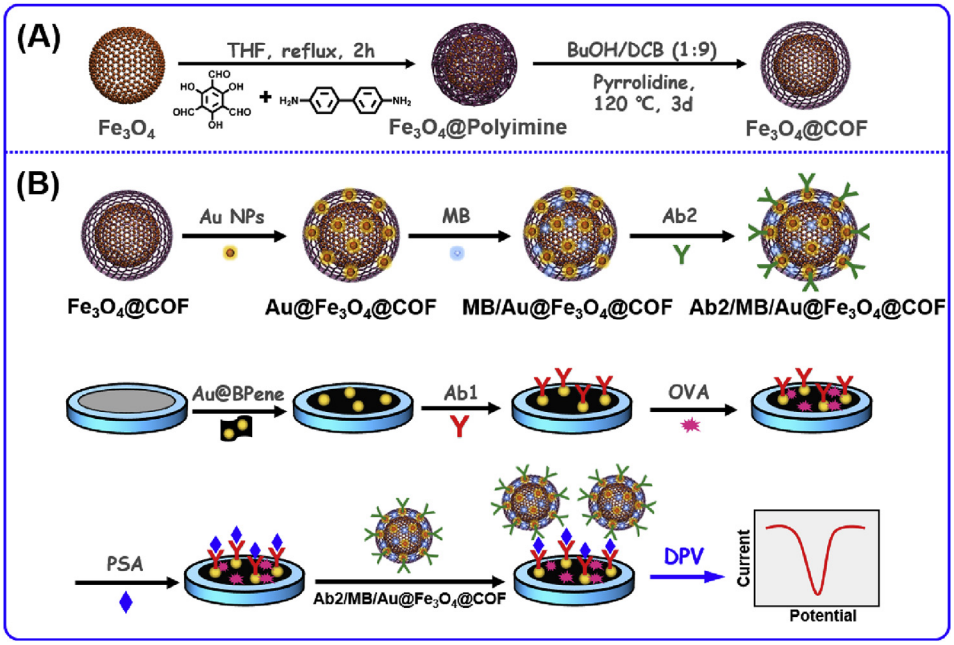

Scheme 1. Synthesis of the Fe_3O_4@COF nanohybrid (**A**) as well as the assembly of the immunosensor for the PSA and signal conversion strategy (**B**).

4 h. The prepared Au@BPene nanomaterial (precipitate) was collected by centrifugation at 10,000 rpm for 20 min and washed thrice with DW. Lastly, Au@BPene nanocomposite was freeze-dried and stored at 4 °C for subsequent use.

2.4. Synthesis of Au NPs loaded Fe_3O_4@COF (Au@Fe_3O_4@COF)

Fe_3O_4 nanocrystal clusters were prepared by a simple chemical method according to a previous work (Li et al., 2018). In brief, 2.70 g of iron chloride hexahydrate, 7.70 g of ammonium acetate, and 0.8 g of sodium citrate were added to 140 mL of ethylene glycol, stirred at 100 °C for 1 h, and then poured into a 200 mL Teflon-lined autoclave. The mixture was heated to 200 °C for 24 h, following which the vessel was naturally cooled to room temperature. Subsequently, the product was poured into a 200 mL beaker and the Fe_3O_4 was separated and collected using a magnet. The precipitate was washed with DW and ethanol thrice. Finally, the black powder product was freeze-dried for further use.

The magnetic COF (Fe_3O_4@COF) materials were synthesized according to a previous procedure (Tan et al., 2016). Briefly, 32 mg of Fe_3O_4 nanocrystal clusters, 22 mL of THF, and 32 mg of BD were added to a beaker via sonication for 15 min and then refluxed with stirring at 50 °C for 30 min. Subsequently, a THF solution of Tp (24 mg, 8 mL) was added dropwise to the above mixture at a rate of 8 drops min^{-1}, following which the mixture was continuously stirred at 50 °C for 12 h. The solvent was then evaporated on a rotary evaporator at 45 °C to obtain the product. Thereafter, 500 μL of 1.0 mg ml^{-1} of Fe_3O_4@COF nanomaterial was dispersed in the above-prepared Au NPs dispersion and stirred at 4 °C for 4 h. The prepared Au@Fe_3O_4@COF nanocomposite was centrifuged at 10,000 rpm for 30 min and washed for thrice with DW. The final product was achieved by freeze drying. X-ray diffraction (XRD) was performed to investigate the crystal properties of Fe_3O_4 and Fe_3O_4@COF.

2.5. Preparation of Ab2/MB/Au@Fe_3O_4@COF bioconjugate (Ab2 bioconjugate)

Initially, 4.0 mL of a 1.0 mg mL^{-1} aqueous solution of MB was added to 10.0 mL of a 1.0 mg mL^{-1} aqueous solution Au@Fe_3O_4@COF and stirred at 4 °C for 12 h. The mixture was then centrifuged for 30 min to remove the excess MB and washed with DW three times. The resulting MB/Au@Fe_3O_4@COF nanocomposite was re-dispersed in 2.0 mL of PBS. Secondly, 100 μL of Ab2 (1.0 mg mL^{-1}) was added to the MB/Au@Fe_3O_4@COF mixture under gentle stirring at 4 °C for 12 h. Thirdly, a 100 μL of 10% BSA solution was added into the above mixture and stirred at 4 °C for 12 h to block nonspecific sites. The product was collected by centrifugation (8000 rpm, 30 min) and washed to remove the unbound Ab2. Finally, the prepared Ab2/MB/Au@Fe_3O_4@COF bioconjugates were dispersed in 1 mL of PBS and stored at 4 °C for further use.

2.6. Fabrication of the modified electrodes

A glassy carbon electrode (GCE, 3 mm in diameter) was polished with 0.3 and 0.05 μm Al_2O_3 powder, respectively, then sonicated in ethanol and DW to remove the substance at the electrode's surface and dried naturally. To prepare the Au@BPene modified electrode, 10 μL of 1.0 mg mL^{-1} Au@BPene dispersion was loaded onto the electrode surface and dried naturally. Subsequently, the Au@BPene immobilised electrode was incubated in 10 μg mL^{-1} of Ab1 at 4 °C for 12 h and washed with PBS to remove the free Ab1. Finally, the Ab1/Au@BPene-modified GCE was incubated in 0.25% OVA for 40 min to block the nonspecific sites and washed with PBS thrice (Yang et al., 2015). The target PSA was then added onto the electrode surface, incubated for another 1 h, and washed with PBS thrice. The PSA/OVA/Ab1/Au@BPene-modified GCE was incubated in the as-prepared aqueous dispersion of Ab2 bioconjugates (Ab2/MB/Au@Fe_3O_4@COF bioconjugates) and washed with PBS three times. Scheme 1 illustrates the synthesis process of the Fe_3O_4@COF nanohybrid as well as the fabrication of the immunosensor. In this study, no more than 20 modified electrodes were treated at the same time.

2.7. Electrochemical measurements

All electrochemical measurements were performed on a CHI660E electrochemical workstation (Shanghai Chenhua, China) using a three-electrode system at the room temperature. Differential pulse voltammetry (DPV) responses of the prepared immunosensors were recorded in PBS in the potential range of 0.2 to −0.6 V with the sensitivity of 1 x 10^{-5} A/V, the pulse amplitude of 0.05 V, and the pulse length of

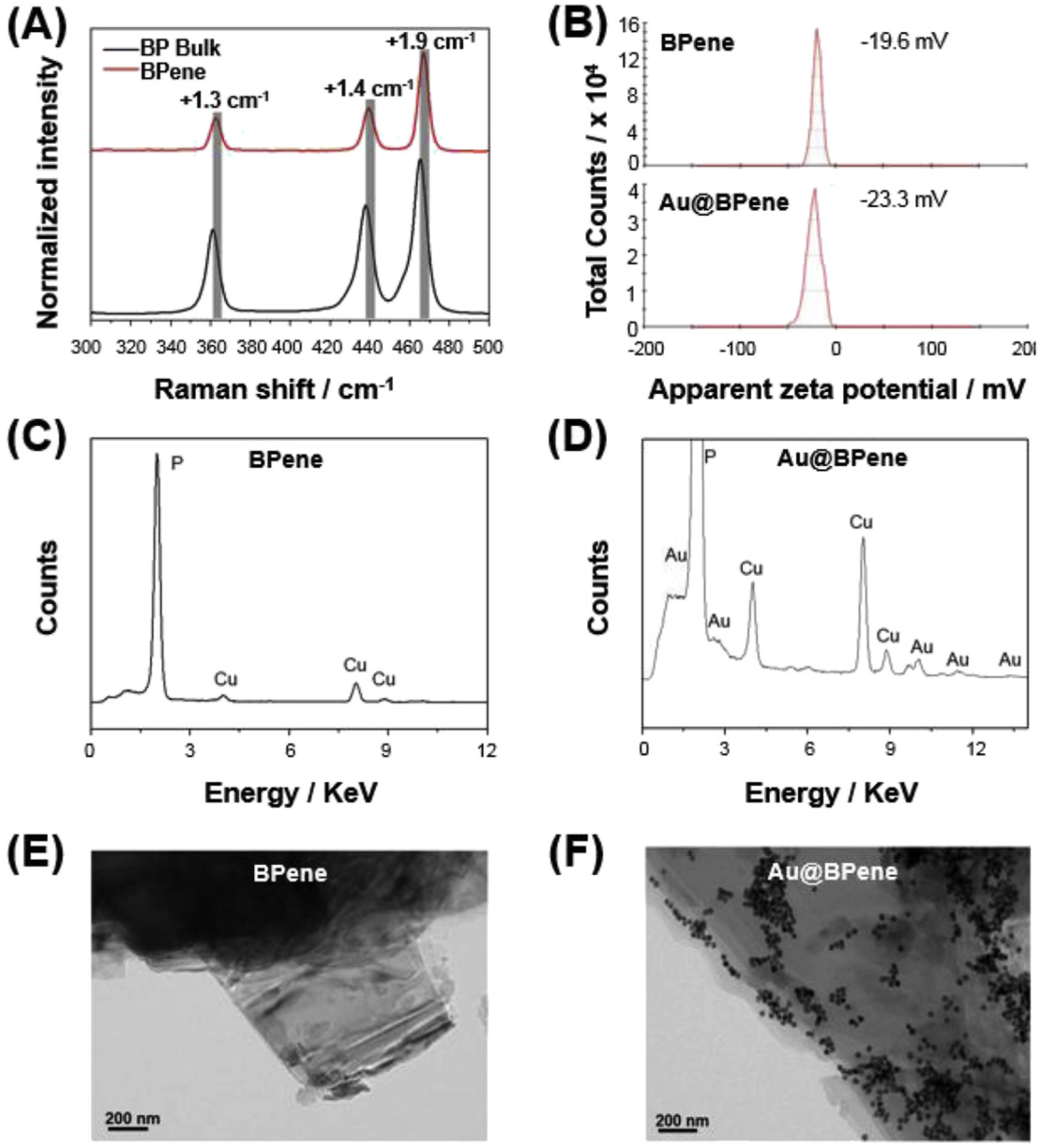

Fig. 1. Characterization of BPene and Au@BPene. Raman spectra of bulk BP and BPene (**A**); Zeta potential of BPene and Au@BPene (**B**); EDX profiles of BPene and Au@BPene (**C, D**); TEM images of BPene and Au@BPene (**E, F**).

0.05 s at a scan rate of 0.05 V/s. The cyclic voltammetry (CV) responses were measured in the potential range from −0.1 to 0.5 V and the sensitivity of 1 x 10^{-5}A/V at a scan rate of 0.1 V/s. Electrochemical impedance spectroscopy (EIS) was performed in the frequency range of 1 x 10^{-1} to 1 x 10^{5} Hz in PBS containing 2 mM $[Fe(CN)_6]^{3-/4-}$ and 0.1 M KCl, and the initial voltage was obtained by measuring the open circuit potential.

3. Results and discussion

3.1. Characterization of BPene and Au@BPene composite

Fig. 1A shows three Raman peak bands appeared at 361, 438, and 466 cm^{-1}, are assignable to the A_g^1, B_{2g}, and A_g^2 optical phonons of bulk BP, respectively. Compared with bulk BP, the distinct Raman peaks of the exfoliated BPene were slightly red-shifted by 1.3, 1.4, and 1.9 cm^{-1}, respectively, attributed to the ultralow thickness of BPene. The EDX profile indicated that BPene was composed of element P (Fig. 1C). Atomic force micrographs (Fig. S1) indicated that the thickness of the exfoliated BPene is ~4.2 nm, suggesting that it was composed of ~ 7 layers according to a previous work (Xia et al., 2014). This result was in good accordance with that reported by Xu et al., who obtained a typical height of ~6–8 layers of BP nanosheets (Xu et al., 2016). TEM images (Fig. 1E) indicated that BPene had a large flat morphology with negative charge (Fig. 1B). These results confirm the successful preparation of an ultrathin nanosheet of BPene.

The Au NP-loaded BPene was then characterized. As shown in Fig. 1B (bottom), after loading the Au NPs with BPene, the zeta potential of BPene became more negative, suggesting that negatively charged Au NPs were successfully loaded onto BPene. Here, the Au NPs are speculated to be adsorbed on the surface of BPene because of the large surface area of Au NPs (Zhao et al., 2017). EDX showed evident signals of elemental Au besides those of P in the Au@BPene nanocomposite (Fig. 1C, D), implying the loading of Au NPs on BPene. Meanwhile, the morphological properties of Au@BPene were further investigated by TEM. Fig. 1E, F clearly shows that the Au NPs were

loaded on the surface of BPene. All results confirmed that the Au NPs were anchored on the surface of BPene, and that the Au@BPene nanocomposite was successfully fabricated.

3.2. Characterization of magnetic COF and Au NPs/magnetic COF composite

FTIR peaks appeared at 586 and 3429 cm^{-1} in Fe_3O_4 respectively, and were assignable to the stretching vibrations of Fe–O and –OH, respectively. Two FTIR peaks at 1452 and 1254 cm^{-1} were observed in Fe_3O_4@COF, attributed to the aromatic C=C and newly formed C–N, suggesting successful synthesis of the COF. The other FTIR peaks of Fe_3O_4@COF were attributed to the stretching vibrations of C=C (1577 cm^{-1}) and aromatic C=O (1623 cm^{-1}) from the COF. Although one of the ligands of the COF (1,3,5-triformyl-2,4,6-trihydroxybenzene) contained –OH, the –OH peak in Fe_3O_4@COF was hardly changed after the synthesis of the COF, implying the successful preparation of the COF. These results were in good agreement with those previously reported (Tan et al., 2016).

Fig. 2B shows the XRD patterns of Fe_3O_4 and Fe_3O_4@COF. Peaks at 30.2°, 35.5°, 53.3°, 57.0°, and 62.6° (2θ) appeared in Fe_3O_4, which were indexed to the crystal structure of Fe_3O_4 according to the standard JCPDS card no. 75–1610. In Fe_3O_4@COF, besides the diffraction peaks of Fe_3O_4, four peaks at 2.1°, 6.0°,18.3° and 26.2° were observed, corresponding to the(100), (200), (210), and (001) reflection planes according to a previous study (Li et al., 2018); this confirms the successful synthesis of Fe_3O_4@COF. The magnetic property of the Fe_3O_4@COF nanoparticles was confirmed by visual observation after magnet treatment. The aqueous dispersion of Fe_3O_4@COF was dark brown, while the Fe_3O_4@COF nanoparticles were attracted around the external magnet and became light brown after treatment with the magnet (Fig. S2). This suggests that although the Fe_3O_4 nanoparticles were covered with the COF layer, their magnetism was retained. To investigate the charge of the material, the zeta-potentials of COF nanomaterials were performed. The average zeta potential of Fe_3O_4@COF was −8.0 mV and that of Au@Fe_3O_4@COF was −30.0 mV (Fig. 2C, E), showing an increased negative potential by −22 mV after Au NPs loading. The increased negative charge was caused by the negatively charged Au NPs. The EDX result showed that Fe, C, and O elements are present in Fe_3O_4@COF, and Au was detected in Au@Fe_3O_4@COF **(**Fig. 2D, F). Fe, C, and O elements are present in Fe_3O_4@COF, and Au is detected in Au@Fe_3O_4@COF. XPS was used to determine the electronic structure and compositions of Au@Fe_3O_4@COF. The survey spectrum confirmed the presence of C, O, N, Fe, and Au in the Au@Fe_3O_4@COF composite, which is in agreement with the XPS results (Fig. S3).

To gain a better understanding of the morphology and structure of the COF, Fe_3O_4@COF, and Au@Fe_3O_4@COF, SEM, TEM, and elemental mapping analyses were performed (Fig. 3). The SEM images showed that flower-like nanosheets of the COF were formed after polymerization (Fig. 3A, D), and Fe_3O_4 nanoparticles were observed in Fe_3O_4@COF (Fig. 3D**).** The TEM images show the size and shape of the Fe_3O_4 and Fe_3O_4@COF. Regular nanoparticles were observed in the Fe_3O_4 sample (Fig. 3B), and the polymer network was deposited on the surface of Fe_3O_4 to form a well-defined Fe_3O_4@COF nanocomposite with a ~ 100 nm thick polymer shell (Fig. 3E). Furthermore, after the assembly reaction, Au NPs were loaded onto the transparent COF in Fe_3O_4@COF (Fig. 3C, F) with an average size of ~ 14 nm (Fig. 3G **a, b**). Elemental mapping analysis indicated that C, O, Au, and N elements were distributed on the surface of Au@Fe_3O_4@COF, demonstrating their coexistence (Fig. 3G **c-f**). All the above results confirmed the successful preparation of the probe Au@Fe_3O_4@COF.

3.3. Characteristics of the modified GCE

To confirm the successful immobilization of the nanocomposite on the GCE, the modified electrode assembly was characterized by EIS and CV. As shown in Fig. 4A**,** compared with the GCE (Fig. 4A**,** curve a), the charge-transfer resistance (Rct) of the Au@BPene-modified GCE decreased markedly (Fig. 4A**,** curve b) because the Au@BPene nanohybrid can increase the charge transfer rate and improve the electrical conductivity of the electrode. When Abl was immobilised onto the Au@BPene-modified GCE, Rct of the electrode increased (Fig. 4A**,** curve c), and following blocking of the nonspecific site using OVA, further increased (Fig. 4A**,** curve d). After incubation with PSA, an additional increase in Rct was observed, implying that the target antigen was successfully bound to the Ab1 loaded on the electrode (Fig. 4A**,** curve e). However, Rct sharply declined after incubation of the Ab2/MB/Au@Fe_3O_4@COF bioconjugates (Fig. 4A**,** curve f), because the Au NPs in the bioconjugates have high conductivity, which is conducive for electron transfer. CV is a useful technique to investigate the electron transfer ability of the electrode. Herein, CV was used to confirm the modification of the electrode surface, and the results are shown in Fig. 4B **and** Table S1. The No. of electrodes (a-f) are same in both Fig. 4B **and** Table S1**.** Compared with the GCE (Fig. 4B**,** curve a), the current of the Au@BPene-loaded GCE increased markedly, and then decreased after incubation with Ab1 (Fig. 4B**,** curves b, c). The current of the Abl/Au@BPene-modified GCE further decreased after blocking the non-specific site with OVA (Fig. 4B**,** curve d). After binding the PSA, the OVA/Abl/Au@BPene-modified GCE showed a significant decrease in the current, to the lowest value (Fig. 4B**,** curve e). However, after conjugation with the Ab2/MB/Au@Fe_3O_4@COF bioconjugates, the peak current increased (Fig. 4B**,** curve f). The CV changes agreed well with the Rct changes, thereby confirming the successful fabrication of the sensing platform.

To test the signal amplification strategy, the CVs responses of various materials-modified electrodes towards MB were studied (Fig. S4). After being modified with material, the electrode was then incubation with 10 μL 10 mM MB solution for 60 min. Then, the free MB was removed by washing 3 times with PBS. The CV of the resulting electrode displayed a pair of redox peaks at around −0.30 V. However, the potential peak slightly negative-shifted using BPene, COF, Fe_3O_4, and Fe_3O_4@COF, suggesting that the MB suffers a reduction to the leuco form in the presence of these materials. Meanwhile, the changes in potential were observed, meaning the less energy was needed for the redox process. Interestingly, among these materials, Fe_3O_4@COF nanocomposite had the highest response towards MB, indicated that it could be used as a signal amplifier. Subsequently, the signal amplification strategy of the immunosensor was further performed using various materials (Fig. S5). In the absence of Au NPs on the surface material (Fig. S5**: column 1, 2**) or probe (Fig. S5**: column 4–6**), the current peaks were lower than the corresponding Au NPs modified electrode, suggested that the Au NPs play important role in signal amplifier. Although the COF, Fe_3O_4, or Fe_3O_4@COF modified probe could somewhat enhance the current signal (Fig. S5**: column 8–10**), the Au@Fe_3O_4@COF nanocomposite showed the highest DPV current (Fig. S5**: column 10**), suggesting the synergetic effects of signal amplification of Au NPs, COF, and Fe_3O_4. Accordingly, Au@Fe_3O_4@COF can be employed as an efficient material for signal amplification and used in the construction of immunosensor for PSA. In this work, Au@Fe_3O_4@COF in principle is a label for the Ab2 enhancing the current signal. MB is considered to enter the framework (pore) of COF to form a stable “host-guest” complex through supramolecular interactions, such as π−π interaction, hydrophobic interaction, and electrostatic interaction. Subsequently, the effect of pH on the current peak of MB was investigated by DPV measurement. The current increased with the increase of pH values from 6.0-7.2, and reached a maximum at pH 7.2. However, the current decreased when pH increased from 7.2 to 8.0 (Figs. S6A and B). Therefore, pH 7.2 was selected as the optimal pH of the immunosensor and used in the following experiments.

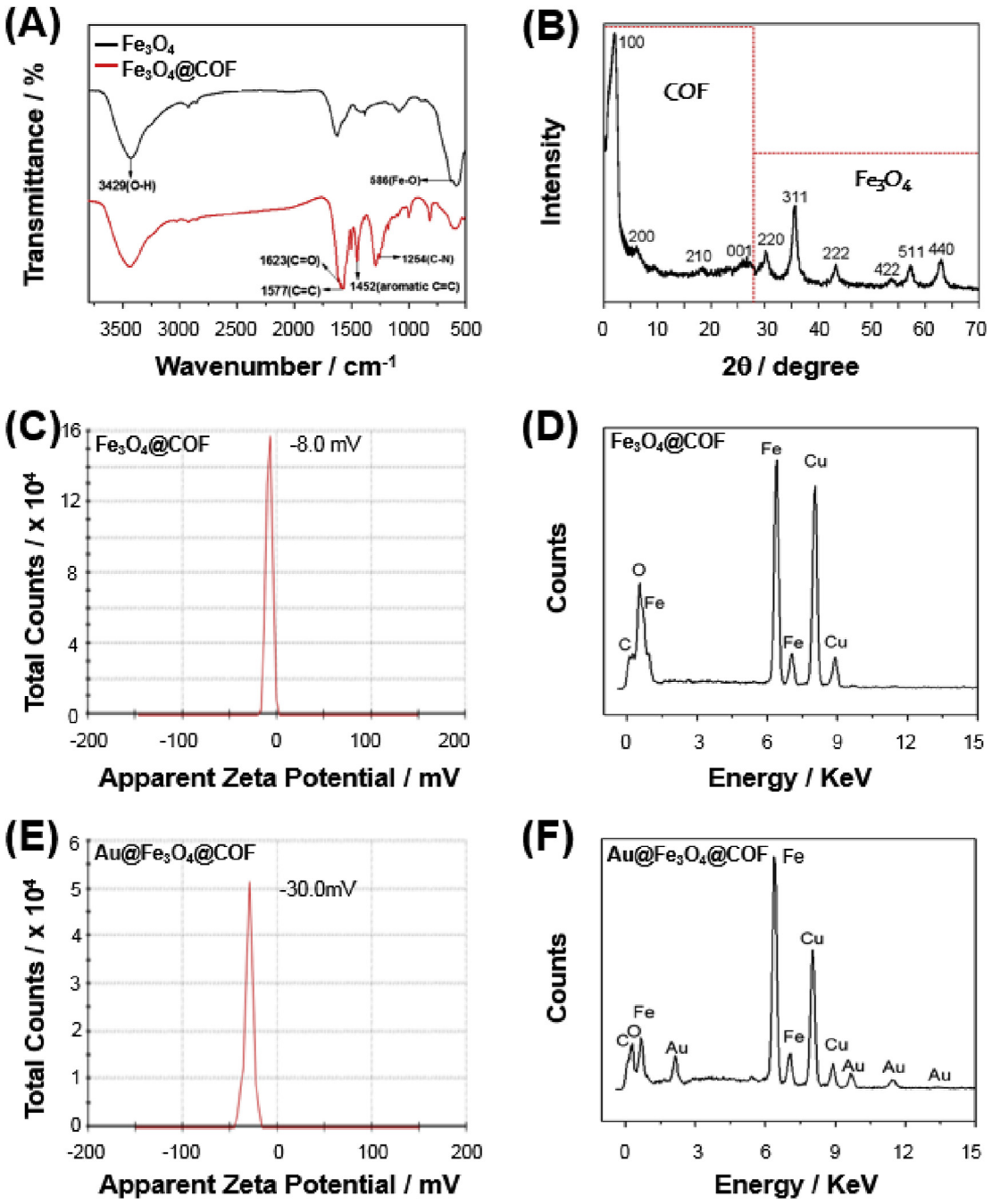

Fig. 2. Characterization of Fe_3O_4@COF and Au@Fe_3O_4@COF. IR spectra of Fe_3O_4 and Fe_3O_4@COF(**A**); XRD survey spectra of Fe_3O_4 and Fe_3O_4@COF (**B**); Zeta potential of Fe_3O_4@COF and Au@Fe_3O_4@COF (**C, E**); EDX profiles of Fe_3O_4@COF and Au@Fe_3O_4@COF (**D, F**).

3.4. Detection of PSA by the fabricated immunosensor

The PSA was determined using the fabricated immunosensor. Fig. 4C shows the DPV curves of Au@Fe_3O_4@COF for various concentrations of the PSA. The reduction peak current of MB at approximately −0.30 V proportionally increased with increasing log concentration of PSA from 0.0001 ng mL^{-1} to 10 ng mL^{-1} (Fig. 4C). The obtained linear relation between the peak current and log concentration of the PSA was $\triangle I$ (μA) = −0.899logC − 6.319 (R^2 = 0.996) with the limit of detection (LOD) of 30 fg mL^{-1} (S/N = 3) (Fig. 4D), providing excellent detection sensitivity compared with previously reported methods (Table 1). Notably, as an aromatic heterocyclic dye, the MB molecule may enter the numerous pores of COF and be stabilized by multiple noncovalent interactions, such as the π−π stacking, hydrophobic, and electrostatic interactions, thereby leading to their enrichment in the COF and consequently, improvement in the electrochemical signal. Meanwhile, Fe_3O_4 can catalyze the electrochemical redox reaction of MB and thus enhance the redox signal. Furthermore, the Au NPs loaded on the nanocomposite were also vital for signal amplification, which is an efficient strategy for signal enhancement. Accordingly, the excellent performance of the fabricated immunosensor is considered to be attributed to the above-mentioned integrated factors. In further study, for the simple and easy application of the constructed immunosensor, miniaturization electrochemical sensing device may be useful for practical application.

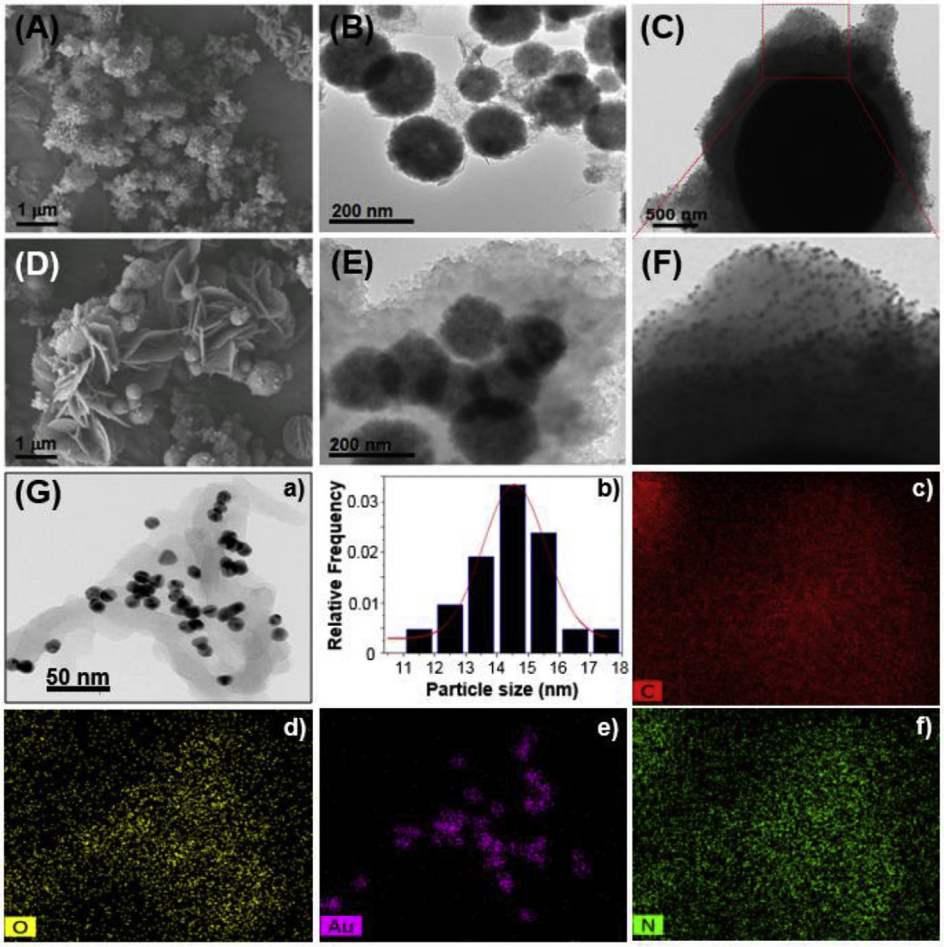

Fig. 3. Electron micrographs and elemental maps. SEM of COF and Fe_3O_4@COF (**A, D**); TEM of Fe_3O_4 and Fe_3O_4@COF (**B, E**); TEM of Au@Fe_3O_4@COF (**C, F**); Elemental mapping of Au@Fe_3O_4@COF. a): TEM of Au@Fe_3O_4@COF (part), b): distribution of particle size of Au NPs onto Au@Fe_3O_4@COF, c): carbon, d): oxygen, e): gold, and f): nitrogen (**G**). (For interpretation of the references to color in this figure legend, the reader is referred to the Web version of this article.)

3.5. Selectivity, repeatability, and stability of the immunosensor

The selectivity of the constructed immunosensor was determined and the results are shown in Fig. S7 **and** Fig. S8A. In the absence of PSA, the DPV peak current of the immunosensor was low, and the non-specific protein (BSA) hardly affected the peak current (Fig. S7), preliminaryly suggested the good selectivity of immunosensor. Furthermore, the specificity of the immunosensor was investigated in the presence of target and non-specific protein (Fig. S8A). In the presence of 1.0 ng mL^{-1} PSA, the peak current of the modified electrode was −6.82 μA. In the presence of individual interferent (hIgG, HSA, Lz, CEA, or CRP 100.0 ng mL^{-1}) or their mixture, the changes in current were lower than 5%, indicating the superior selectivity of the immunosensor for PSA determination. Next, the repeatability of the immunosensor was evaluated by measuring the peak current of the six modified electrodes to detect 1 ng mL^{-1} PSA. Fig. S8B shows that the relative standard deviation (RSD) of the response current is 2.03%, illustrating its acceptable repeatability. In terms of stability, after being stored in a commercial refrigerator at 4 °C in 15 d, the current response of the modified electrodes was maintained at more than 95.5% of the initial response (Fig. S8C), demonstrating the good stability of the sensors. It is worthy to note that the proposed electrochemical immunosensor needs less volume of sample but longer analysis time compared with ELISA assay (Table S2).

3.6. Determination of the PSA in serum

To investigate the potential application of the proposed immunosensor, the PSA concentration in human serum samples was determined using a standard addition assay. Various concentrations of PSA (0.5, 1, and 5.0 ng mL^{-1}) were added to the serum samples, and the corresponding results are shown in Table S3**.** The recoveries of the sensor ranged from 96.3% to 104.6%, with the RSD ranging from 1.1% to 4.6%. This highlights the potential application of the sensor in clinical diagnosis.

4. Conclusion

In summary, we have developed a novel electrochemical sensing platform for the PSA based on BPene and a magnetic COF. The fabricated sensor exhibited a linear range from 0.0001 ng mL^{-1} to 10 ng mL^{-1}, with an LOD of 30 fg mL^{-1}. The sensor was successfully used to determine the PSA in real samples with high specificity, good stability, and desirable reproducibility. The designed strategy has potential applications in the detection of cancer biomarkers in clinical diagnostics. Since the detection time of the immunosensor in this work are still long, further attempts are needed to overcome this disadvantage. Meanwhile, development of miniaturized thick- or thin-film, e.g. screen-printing electrode and electrochemical device may be crucial for the practical application in clinical diagnosis, which is in progress in our laboratory.

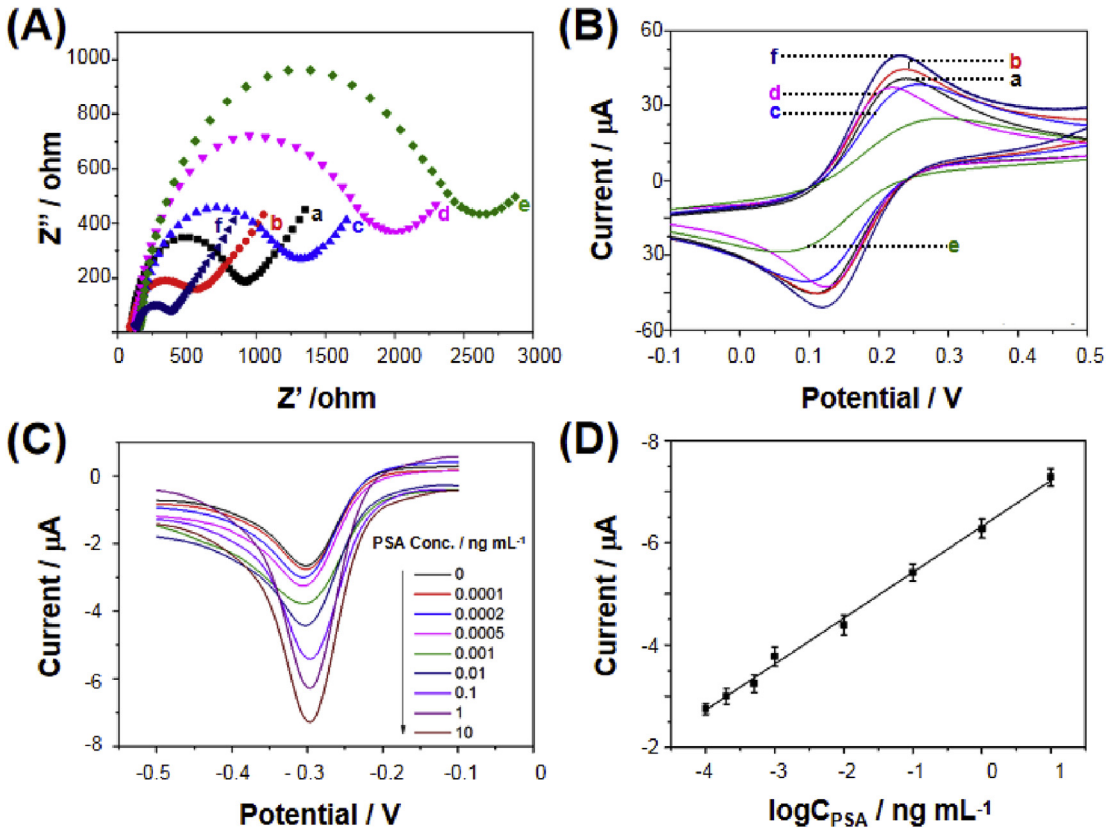

Fig. 4. Assembly of modified electrodes characterized by EIS (**A**) and CV (**B**) in 0.1 M PBS containing 2.0 mM $[Fe(CN)_6]^{3-/4-}$ and 0.1 M KCl: a, GCE; b, Au@BPene@GCE; c, Ab1/Au@BPene@GCE; d, OVA/Ab1/Au@BPene@GCE; e, PSA/OVA/Ab1/Au@BPene@GCE; f, Ab2/MB/Au@Fe_3O_4@COF-PSA/OVA/Ab1/Au@BPene@GCE; EIS was performed in the frequency range of 10^{-1} to 10^{-5} Hz with an amplitude of 5 mV. DPV curves for different concentrations of PSA in 0.1 M PBS (**C**). Calibration plot for log[$C_{PSA,}$ ng mL^{-1}] *vs.* DPV response in the range of 0.0001 to 10 ng mL^{-1}. Error bar = standard deviation (SD),(n = 5) (**D**).

CRediT authorship contribution statement

Huan Liang: Conceptualization, Data curation, Investigation, Project administration, Supervision, Validation, Writing - original draft. **Hanbin Xu:** Conceptualization, Project administration, Supervision, Validation. **Yuting Zhao:** Supervision, Validation, Writing - review & editing. **Jing Zheng:** Supervision, Validation, Writing - review & editing. **Hui Zhao:** Conceptualization, Project administration, Supervision, Validation, Writing - review & editing. **Guoliang Li:** Conceptualization, Supervision, Validation, Writing - review & editing. **Can-Peng Li:** Conceptualization, Project administration, Supervision, Validation, Funding acquisition.

Declaration of competing interest

The authors declare that they have no known competing financial interests or personal relationships that could have appeared to influence the work reported in this paper.

Acknowledgements

This work was financially supported by the National Natural Science Foundation of China (21764005, 21565029), Key Projects of Yunnan Natural Science Foundation (2018FA005), Key Research and Development Projects of Yunnan (2018BC005), Program for Excellent Young Talents of Yunnan University, and the Program for Donglu Scholars of Yunnan University.

Appendix A. Supplementary data

Supplementary data to this article can be found online at https://doi.org/10.1016/j.bios.2019.111691.

Table 1
Comparison of different electrochemical immunosensors for PSA detection.

Electrode	Method	Linear range (ng mL^{-1})	LOD (ng mL^{-1})	Reference
SP/rGO/GCE	DPV	0.1–5.0, 5.0–80	0.053	Wang et al., (2015)
Au/Pd@flower-like SnO_2/GCE	DPV	0.01–100	0.030	Yang et al., (2015)
Au/GR/GCE	CV	1.0–10	0.59	Jang et al., (2015)
Dendrimer/ILs/CNTs/GCE	DPV	0.05–80	0.001	Kavosi et al., (2014)
AuPd/Au NCs/GCE	DPV	0.1–50	0.078	Wang et al., (2018)
GO/Ag NPs/SPCE	EIS	1.0–1000	0.01	Han et al., (2017)
M-CeO_2/CMC/ILs/GCE	DPV	0.0005–50	0.00016	Wei et al., (2017)
CNT/PAMAM/β-CD/GCE	CV	0.001–30	0.00078	Xie et al., 2015,
Ag NPs/MSNs/GCE	CV	0.05–50	0.015	Wang et al., (2013)
Au NPs/BPene/Fe_3O_4–COF/GCE	DPV	0.0001–10	0.00003	This work

References

Cesaro－Tadic, S., Dernick, G., Juncker, D., Buurman, G., Kropshofer, H., Michel, B., Fattinger, C., Delamarche, E., 2004. Lab Chip 4, 563–569.

Center, M.M., Jemal, A., Lortet-Tieulent, J., Ward, E., Ferlay, J., Brawley, O., Bray, F., 2012. Eur. Urol. 61, 1079–1092.

Cheng, Z., Choi, N., Wang, R., Lee, S., Moon, K.C., Yoon, S.-Y., Chen, L., Choo, J., 2017. ACS Nano 11, 4926–4933.

Colson, J.W., Dichtel, W.R., 2013. Nat. Chem. 5, 453–465.

Cooperberg, M.R., Brooks, J.D., Faino, A.V., Newcomb, L.F., Kearns, J.T., Carroll, P.R., Dash, A., Etzioni, R., Fabrizio, M.D., Gleave, M.E., Morgan, T.M., Nelson, P.S., Thompson, I.M., Wagner, A.A., Lin, D.W., Zheng, Y., 2018. Eur. Urol. 74, 211–217.

Côté, A.P., Benin, A., Ockwig, N.W., Keeffe, M.O., Matzger, A.J., Yaghi, O.M., 2005. Science 310, 1166–1170.

Ding, S.Y., Gao, J., Wang, Q., Zhang, Y., Song, W.G., Su, C.Y., Wang, W., 2011. J. Am. Chem. Soc. 133, 19816–19822.

Fang, Q., Gu, S., Zheng, J., Zhuang, Z., Qiu, S., Yan, Y., 2014. Angew. Chem., Int. Ed. Engl. 53, 2878–2882.

Ge, X., Xia, Z., Guo, S., 2019. Adv. Funct. Mater. 1900318, 1–32.

Han, L., Liu, C.M., Dong, S.L., Du, C.X., Zhang, X.Y., Li, L.H., Wei, Y., 2017. Biosens. Bioelectron. 87, 466–472.

He, S., Zeng, T., Wang, S., Niu, H., Cai, Y., 2017. ACS Appl. Mater. Interfaces 9, 2959–2965.

Jang, H.D., Kim, S.K., Chang, H., Choi, J.W., 2015. Biosens. Bioelectron. 63, 546–551.

Jin, G., Wang, C., Yang, L., Li, X., Guo, L., Qiu, B., Lin, Z., Chen, G., 2015. Biosens. Bioelectron. 63, 166–171.

Kavosi, B., Salimi, A., Hallaj, R., Amani, K., 2014. Biosens. Bioelectron. 52, 20–28.

Li, J.R., Sculley, J., Zhou, H.C., 2012. Chem. Rev. 112, 869–932.

Li, L., Yu, Y., Ye, G.J., Ge, Q., Ou, X., Wu, H., Feng, D., Chen, X.H., Zhang, Y., 2014. Nat. Nanotechnol. 9, 372–377.

Li, P., Zhang, D., Liu, J., Chang, H., Sun, Y., Yin, N., 2015. ACS Appl. Mater. Interfaces 7, 24396–24402.

Li, P., Zhang, D., Jiang, C., Zong, X., Cao, Y., 2017. Biosens. Bioelectron. 98, 68–75.

Li, N., Wu, D., Hu, N., Fan, G., Li, X., Sun, J., Chen, X., Suo, Y., Li, G., Wu, Y., 2018. J. Agric. Food Chem. 66, 3572–3580.

Liu, T.Z., Hu, R., Zhang, K.L., Liu, Y., Zhang, X.B., Bai, R.Y., Li, D.L., Yang, Y.H., 2016a. Anal. Chem. 88, 12516–12523.

Liu, Y., Yuan, X., Zhang, C., Jin, Z., Narayan, A., Luo, C., Chen, Z., Yang, L., Zou, J., Wu, X., Sanvito, S., Xia, Z., Li, L., Wang, Z., Xiu, F., 2016b. Nat. Commun. 7, 12516 1－8.

Luo, M., Fan, T., Zhou, Y., Zhang, H., Mei, L., 2019. Adv. Funct. Mater. 29, 1808306.

Pei, H., Zhu, S., Yang, M., Kong, R., Zheng, Y., Qu, F., 2015. Biosens. Bioelectron. 74, 909–914.

Tan, J., Namuangruk, S., Kong, W.F., Kungwan, N., Guo, J., Wang, C.C., 2016. Angew. Chem. Int. Ed. 55, 13979–13984.

Teppo, A.M., Maury, C.P., 1987. J. Clin. Chem. 33, 2024–2027.

Wang, H., Zhang, Y., Yu, H.Q., Wu, D., Ma, H.M., Li, H., Du, B., Wei, Q., 2013. Anal. Biochem. 434, 123–127.

Wang, Y.Y., Qu, Y., Liu, G.S., Hou, X.D., Huang, Y.N., Wu, W.Z., Wu, K.B., Li, C.Y., 2015. Microchim. Act. 182, 2061–2067.

Wang, J., Li, J., Gao, M., Zhang, X., 2017. Nanoscale 9, 10750–10756.

Wang, R., Liu, W.D., Wang, A.J., Xue, Y.D., Wu, L., Feng, J.J., 2018. Biosens. Bioelectron. 99, 458–463.

Wei, Y.C., Li, X.J., Sun, X., Ma, H.M., Zhang, Y., Wei, Q., 2017. Biosens. Bioelectron. 94, 141–147.

Wen, T., Zhu, W., Xue, C., Wu, J., Han, Q., Wang, X., Zhou, X., Jiang, H., 2014. Biosens. Bioelectron. 56, 180–185.

Xia, F., Wang, H., Jia, Y., 2014. Nat. Commun. 4458, 1–6.

Xie, S.B., Zhang, J., Yuan, Y.L., Chai, Y.Q., Yuan, R., 2015. Chem. Commun. 51, 3387–3390.

Xu, J.Y., Gao, L.F., Hu, C.X., Zhu, Z.Y., Zhao, M., Wang, Q., Zhang, H.L., 2016. Chem. Commun. 52, 8107–8110.

Xuan, Z., Li, M., Rong, P., Wang, W., Li, Y., Liu, D., 2016. Nanoscale 8, 17271–17277.

Yan, X., Song, Y., Liu, J., Zhou, N., Zhang, C., He, L., Zhang, Z., Liu, Z., 2019. Biosens. Bioelectron. 126, 734–742.

Yang, L., Zhao, H., Deng, G.G., Ran, X., Li, Y.C., Xie, X.G., Li, C.P., 2015. RSC Adv. 5, 74046–74053.

Yang, L., Ran, X., Cai, L., Li, Y., Zhao, H., Li, C.P., 2016. Biosens. Bioelectron. 83, 347–352.

Yang, Y., Yan, Q., Liu, Q., Li, Y., Liu, H., Wang, P., Chen, L., Zhang, D., Li, Y., Dong, Y., 2018. Biosens. Bioelectron. 99, 450–457.

Zeng, X.W., Luo, X.X., Liu, G., Wang, X.S., Tao, W., Lin, Y.X., Ji, X.T., Nie, L., Mei, L., 2018. Adv. Sci. 5, 1–8.

Zhang, T., Ma, N., Ali, A., Wei, Q., Wu, D., Ren, X., 2018. Biosens. Bioelectron. 119, 176–181.

Zhao, H., Liu, F., Wu, S., Yang, L., Zhang, Y.P., Li, C.P., 2017. Nanoscale 9, 4272–4282.

Zhao, Y., Zhang, Y.H., Zhuge, Z., Tang, Y.H., Tao, J.W., Chen, Y., 2018. Anal. Chem. 90, 3149–3155.

Zhao, H., Liu, F., Lu, Y.X., Jin, L., Tan, S., Zhang, Y.P., Li, C.P., 2019. Sens. Actuators, B 285, 553–561.